Unsteady computational fluid dynamics analysis of the hydrodynamic instabilities in a reversible Francis turbine used in a storage plant

S. Mauro [a],[*], R. Lanzafame [a], S. Brusca [b], M. Messina [a]

[a] Department of Civil Engineering and Architecture, University of Catania, Via Santa Sofia 64, 95123, Catania, Italy
[b] Department of Engineering, University of Messina, Contrada Di Dio, 98166, Messina, Italy

ARTICLE INFO

ABSTRACT

The hydraulic storage plants play a strategic role in the management of large electrical networks. Besides the widely known capability to store and provide great amount of energy, in a green and efficient way, these plants are of utmost importance to guarantee the perfect balance of the Italian electricity grid. For this reason the reversible turbomachineries, used in these plants, are subjected to a particularly intensive use which strongly affects their reliability. The present work deals with a real issue of the ENEL Green Power "Anapo" storage hydro plant, located in Sicily (Italy). In this plant strong and increasing vibrations were detected in the Fink's guide vane, particularly during the pumping operating conditions. In order to find the sources of these vibrations and for a quantitative evaluation of the structural loads on the Fink's guide vane blades, an unsteady CFD 3D model of the reversible turbine was implemented and validated using data provided by ENEL. The model accurately reproduced the hydrodynamic behavior of the water flow within the entire machinery, between the Kaplan's diffuser and the spiral case. This allowed for the calculation of the time dependent trend of the structural loads over the Fink's vane blades. The frequencies and the amplitudes of the loads were analyzed through the use of a Fast Fourier Transformation. Moreover, the CFD model allowed for a sensitivity study of the guide vane opening angle effects. This study provides an interesting insight into the hydrodynamic behavior of the machine.

1. Introduction

The ever increasing contribution of renewable energy in the electrical grids is becoming a great problem for their stability. Above all wind energy is very variable in time and when it is massively delivered to the grid a lot of control problems arise [1, 2]. This is due to the fact that a grid must be in a perfect balance between instantaneous electrical power demand and production in order to maintain a constant network frequency. In this scenario, the hydraulic storage plants play an ever more strategic role for the management of the network stability [3, 4, 5], thanks to their capability to store and provide great amount of electrical energy in very short time, using reversible turbomachineries. However, this implies a much heavier use of the turbomachineries of the storage plants which have been often used for thirty or forty years and therefore they are nowadays subjected to increasing reliability and fatigue problems. Furthermore, the design of such hydro-turbomachineries dates back to a period when no advanced 3D calculation codes were available and the machineries were designed using simplified 1D models and empirical corrections. This may leave a margin of optimization which

would result in a reduction of the fatiguing loads and possible improvements of the machine efficiency. With the advent of modern 3D CFD codes and the increasing computation capabilities, a renewed interest toward the fluid dynamic modeling of these turbomachineries would be desirable to meet the needs of the electrical power industry as well. Indeed, since these storage plants are so strategic, also from an economic point of view, the failure of even just one turbomachinery would be a serious problem for both the electrical network stability and the economics of the electrical industries. For the same reasons, another important issue is related to the fact that it is not possible to stop the turbomachineries for an experimental investigation of the causes which lead to reliability problems. Therefore, the possibility to develop unsteady CFD 3D models of the turbomachineries allows for an accurate virtual inspection of their hydrodynamic behavior. This in turn is a great help for the detection of the possible causes of reliability and fatiguing problems without the necessity to stop the activities of the plant.

According to what has just been said, the present paper deals with a real problem of the "Anapo" ENEL Green Power storage hydro plant located in Sicily (Italy). The "Anapo" hydro plant is one of the most
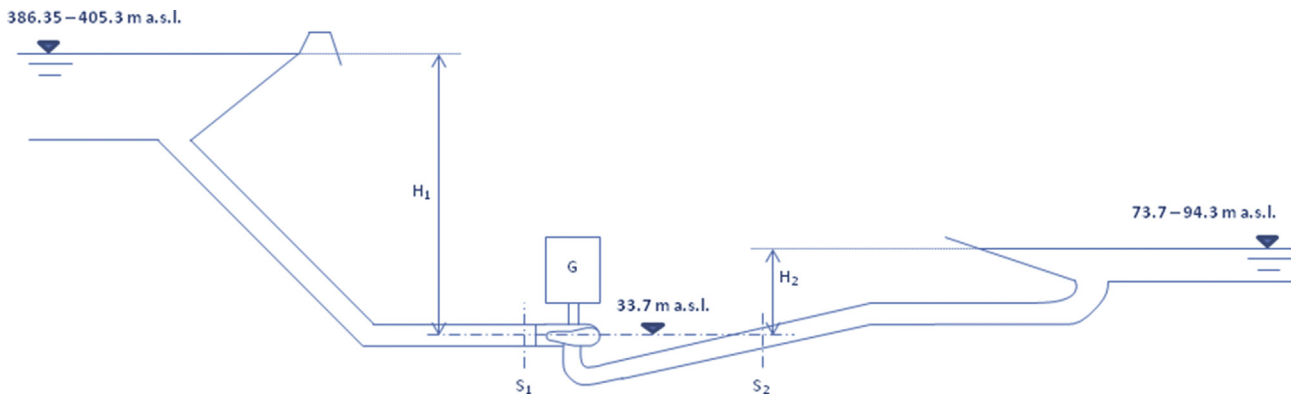

Fig. 1. "Anapo" storage plant layout with upper basin water level H_1, lower basin water level H_2, turbomachinery group G and simulated sections S_1 and S_2.

Table 1
Reversible Francis turbine features (Courtesy of ENEL Green Power).

Manufacturer	Hydroart-Riva 1982
Minimum diameter impeller	2.185 [m]
Maximum diameter impeller	3.55 [m]
Inlet blade height	0.4 [m]
Number of impeller blades	7
Number of stay vane blades	10
Number of guide vane blades	20
Rotational speed	428.57 [r/min]
Turbine head range	285.26–328.12 [m]
Turbine volumetric flow-rate range	48.18–52.81 [m³/s]
BPE turbine head	311 [m]
BPE turbine volumetric flow-rate	52 [m³/s]
Turbine power range	116.63–150.81 [MW]
Turbine global efficiency range	86.5–90.6 [%]
Pump head range	294.96–335.81 [m]
Pump volumetric flow-rate range	37.29–45.49 [m³/s]
BPE pump head	311 [m]
BPE pump volumetric flow-rate	40 [m³/s]
Pump power range	135.44–147.56 [MW]
Pump global efficiency range	89.2–90.7 [%]

important storage plant in Italy. In Fig. 1 a schematic layout of the global hydraulic system is presented.

The upper basin has a storage capacity of 5,600,000 m³ and its level can oscillate between 386.35 m and 405.3 m above sea level (a.s.l.). The lower basin has a capacity of 7,300,000 m³ and its level oscillates between 73.7 m and 94.3 m above sea level. The turbomachinery group is schematized between sections S_1 and S_2 and is located below the lower basin level at 33.7 m a.s.l. The motor-generator group is indicated with G. The plant has four reversible Francis hydro turbines manufactured by Hydroart/Riva in 1982. The characteristics of each turbomachinery are

reported in Table 1.

During the last years, due to the massive increase of renewable energy on the Italian grid, the "Anapo" storage plant has been subjected to heavier use. At the same time, the guide vane (GV) blades have begun to be affected by strong and increasing vibrations which have led to the failure of one of the four groups with great economic damages. Since the vibrations may be related to hydrodynamic instabilities, in order to investigate the possible sources, the authors developed an unsteady CFD 3D model of the full Francis turbine, under pumping condition, between the flanges S_1 and S_2 (Fig. 1), using the ANSYS Fluent solver. The flange S_1 corresponds to the spiral case inlet while the flange S_2 corresponds to the Kaplan's diffuser outlet. Being the pumping condition the one in which critical vibrations were measured, an experimental pumping operating conditions was used as reference for the validation of the model. Specifically, the model was validated comparing both the numerical and measured volumetric flow-rate and power. Once having validated the numerical model, the time-dependent forces, which act on the guide vane blades, were individually sampled and post-processed using a Fast Fourier Transformation (FFT). Furthermore, several simulations were carried out in order to understand the influence of the GV blade angle on the time-dependent loads and on the efficiency of the machinery. This was done also in order to verify if the use of an accurate CFD 3D approach might have led to a better compromise between efficiency and load reduction on the GV blades. More details about the CFD modeling procedure and validation are presented in the next section.

2. Methodology

2.1. Computational domain and meshing generation

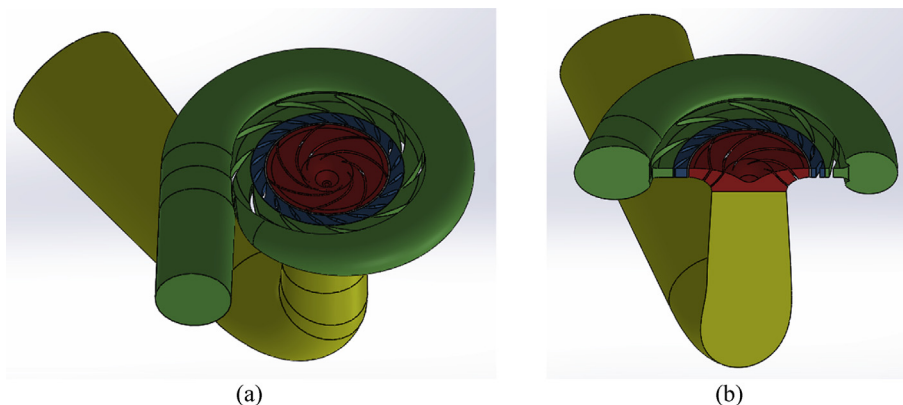The CFD 3D model developed for the present study must be an

Fig. 2. 3D CAD of the fluid dynamic domain of the full reversible Francis turbine (a), axial section of the 3D fluid dynamic domain (b).

Table 2

Grid and time step sensitivity study results.

Grid features	Grid 1			Grid 2			Grid 3		
Spiral case max volume sizing [m]	0.3								
Draft tube max volume sizing [m]	0.2								
Global growth rate [-]	1.2								
Stay vane max volume sizing [m]	0.1								
Rotor volume sizing [mm]	40			20			10		
Guide vane volume sizing [mm]	20			10			5		
Guide vane blade face sizing [mm]	2			1			0.5		
Inflation layers on vane blades	-			5			10		
Y^+ min	38			35			34		
Total elements	≈5 million			≈14 million			≈29 million		
Max skewness	0.92			0.88			0.87		
Time steps [s]	$8 \cdot 10^{-4}$	$4 \cdot 10^{-4}$	10^{-4}	$8 \cdot 10^{-4}$	$4 \cdot 10^{-4}$	10^{-4}	$8 \cdot 10^{-4}$	$4 \cdot 10^{-4}$	10^{-4}
Iterations per time step [-]	40								
Angular step [deg]	2	1	0.25	2	1	0.25	2	1	0.25
Average power [MW]	113.5	118.4	118.1	120.2	130.1	130.3	121.4	130.7	130.8
Average force on blade 1 [kN]	16.7	18.2	18.5	22.1	28.2	28.4	23.4	28.9	28.8
Calculation time per revolution [h]	≈14	≈25	≈48	≈39	≈70	≈134	≈81	≈145	≈278
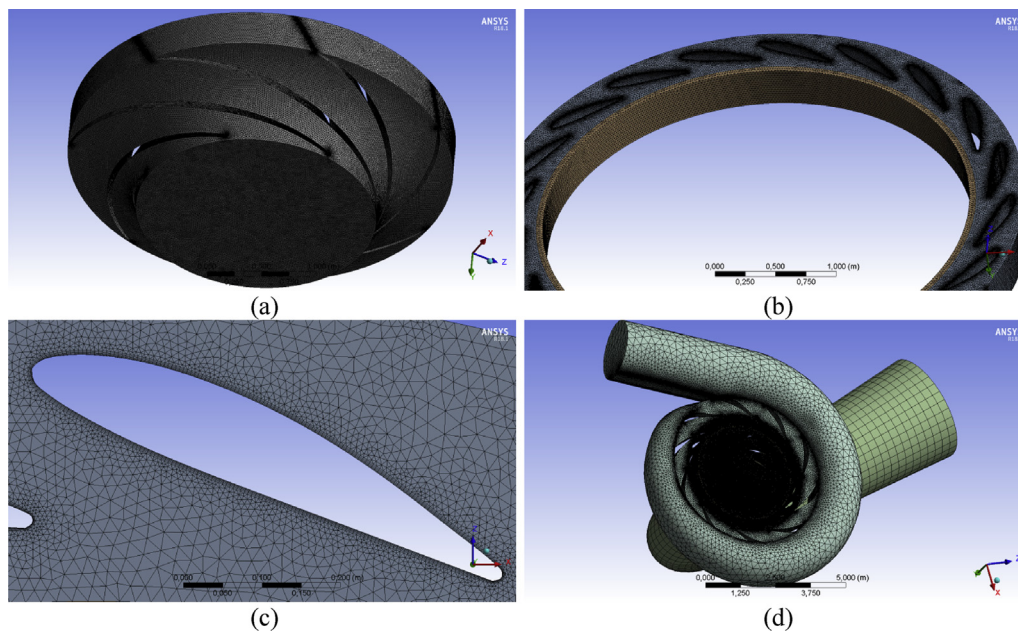
Fig. 3. Details of the mesh (Grid 2) for the rotor (a), the guide vane (b), the guide vane blade section (c) and global view of the entire domain (d).

unsteady model of the full Francis turbine in such a way to investigate the rotor-stator interaction and the time dependent loads which acted on the GV blades. The model was implemented in ANSYS Fluent, following some literature suggestions, above all regarding the turbulence model closure of the RANS equations. Specifically, Teran et al. [6] implemented a CFD model for the optimization of a 500 kW Francis turbine. They used the SST k-ω turbulence model with a steady state solver with very satisfactory numerical-experimental validation. Nicolle et al. [7] simulated the startup of a Francis turbine using a transient CFD model in ANSYS CFX. No details were provided about the turbulence modeling, however they simulated the guide vane blades opening phase with accurate results. Shukla et al. [8] used the ANSYS CFX steady state CFD solver for a detailed investigation of the 3D flows in a Francis turbine demonstrating good agreement between numerical and experimental results. Similar results were obtained from Khare et al. [9]. Trivedi et al. [10] provided a detailed description of the development of a CFD model for the analysis of a Francis turbine at different operating conditions. They used both the k-ε and SST k-ω turbulence model demonstrating very comparable results. Wu et al. [11] performed a CFD study for the validation of an optimization study on Francis turbines using STAR-CD

commercial software and k-ε turbulence formulation for RANS closure. Choi et al [12] implemented a CFD model for the performance optimization of a 500 kW Francis turbine using a tetrahedral mesh and the SST k-ω turbulence model. They showed the great potentialities of the CFD modeling for the 3D flow-field optimization in hydro turbines. Finally Trivedi and Cervantes [13] provided a state of the art in the CFD modeling of Francis turbines evaluating the influence of near wall treatment and turbulence modeling on efficiency, torque, pressure and velocity calculations. Their results demonstrated that the SST k-ω turbulence model led to accurate prediction only when the near wall grid is fine enough to have $y^+ < 1$, as expected. They suggested the use of advanced k-ε models, without near wall treatment and $y^+ > 30$ in order to achieve equally accurate results but with a great save of number of cells and therefore computation time. Moreover, Shah et al. [14] reviewed the state of the art in the CFD modeling of centrifugal pumps which is the objective of the present study as the Francis turbine was simulated in pumping operating condition. The Unsteady RANS equations together with the two equation k-ε turbulence model were found to be the best compromise between accuracy and computation time.

In light of the above, in the present work the first step was to

Table 3
ANSYS Fluent solver set-up.

| Grid elements	≈14 million (Grid 2)	
Time step	0.0004 s (1 deg per time step)	
Sub-iterations per time step	40	
Solution Methods	Solver	Transient Pressure Based SIMPLE
	Discretization methods	Least Squares Cell Based method for gradients Second order upwind discretization for equations Second order implicit for transient formulation
Solution Controls	Relaxation factors	Pressure 0.3 Momentum 0.4
Rotational Model	Sliding Mesh Model (SMM)	
Turbulence Model	RNG k-ε	
Boundary Conditions	Pressure Inlet	570 kPa
	Pressure Outlet	3.62 MPa
	Rotational speed	n = 428.57 [r/min]
Turbulence boundary conditions	Inlet	Tu = 5 % - TVR = 10
	Outlet	Tu = 5 % - TVR = 10
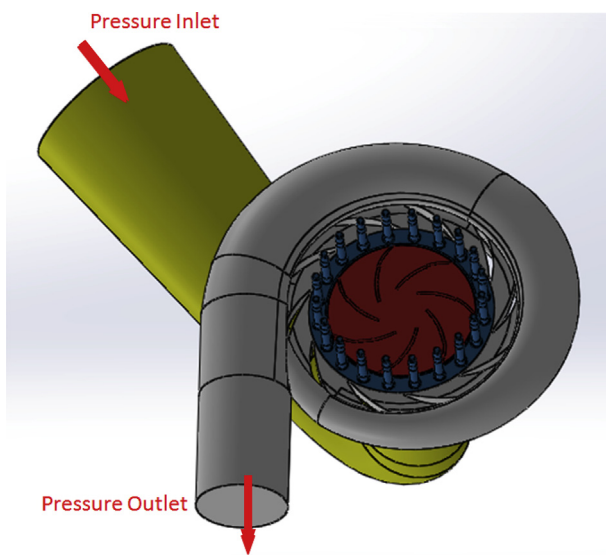
Fig. 4. Location of inlet and outlet boundary conditions on CFD domain.

Table 4
Numerical and experimental validation data.

Test case features	Measured	CFD simulated
Guide vane opening angle [deg]	18	18
Rotational speed [r/min]	428.57	428.57
Inlet pressure head (S_2) [kPa]	570	570
Outlet pressure head (S_1) [MPa]	3.62	3.62
Mass flow rate [kg/s]	40,000	39,665
Mass flow rate relative error [%]	-	-0.84
Absorbed hydraulic power [MW]	132.02	130.08
Power relative error [%]	-	-1.47
Average inlet velocity (S_2) [m/s]	3.35	3.35
Average outlet velocity (S_1) [m/s]	10.53	10.56
Hydraulic efficiency [-]	0.94	0.946

reproduce the CAD geometry of the machine, starting from old 2D technical drawings provided by ENEL. Specifically, the technical drawings consisted of different 2D views and sections of the entire machine (frontal and cross sections, cylindrical and conical sections), including the impeller, by which it was possible to faithfully reconstruct all the 3D
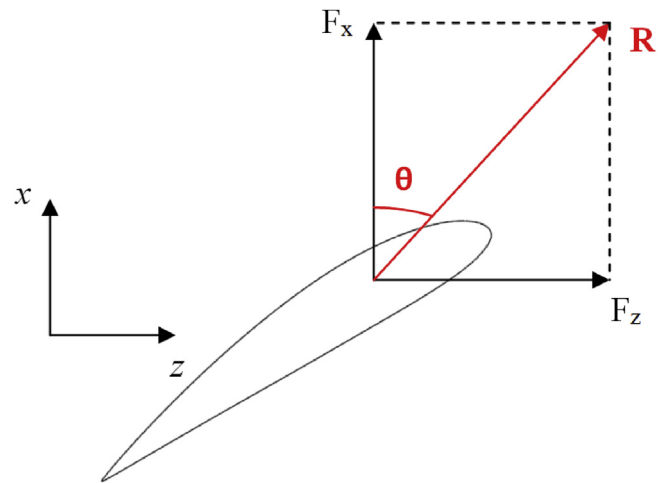
Fig. 5. Frame of reference for the calculation of the magnitude (R) and angle (θ) of the hydrodynamic resultant.

geometries. Then the fluid dynamic domain was generated taking into account all the details which were relevant for the hydro-dynamic simulation. In Fig. 2, two images of the fluid dynamic domain are presented. The CFD domain reproduced the fluid dynamics between sections S_1 and S_2 in Fig. 1.

Four sub-domains are evidenced in Fig. 2. The spiral case together with the stay vane (SV) blades are in green, the Fink's GV is in blue, the impeller is in red and the Kaplan's draft tube is in yellow. The guide vane blade was set in the CAD in the exact angular position of the experimental test case, 18° from the full closed position. The angular position of the GV blades is of utmost importance for the correct evaluation of the time-dependent loads. For this reason, six more CADs were made by changing only the GV angular position from 15° to 21° in order to have the geometries for the aforementioned sensitivity study about the influence of the GV angular position on loads and efficiency.

The next step was to generate the adequate spatial discretization for the specific fluid dynamic problem. A grid independence study was carried out for this purpose. Three grid refinements were tested using ANSYS Meshing software [15, 16]. Details of the mesh sensitivity study are reported in Table 2. Specifically, the refinements were made in the area of high gradients such as the impeller, the rotor-stator interface and the GV domain. The reference parameters used for the independency evaluation were the power at the shaft and the time-averaged force on a GV blade. Being an unsteady simulation, at the same time a time step sensitivity study was necessary and is presented in Table 2 as well. The operating conditions, used for the sensitivity study were those related to the experimental test case provided by ENEL and they are presented hereinafter (Table 4).

The mesh sensitivity study was implemented for the specific test case condition (Table 4) which had an on-design operating guide vane angle of 18°. Then the same grid settings were applied to the other guide vane opening angles, thus resulting in seven different simulation cases. In detail, the meshing strategy was to develop specific settings for each of the domains evidenced in Fig. 2. For the draft tube, an automatic sweep method was used in order to generate high quality hexahedral elements. The maximum element dimension for the draft tube was equal for each of the three grids as reported in Table 2. For the spiral case domain, which contained the SV blades, only global sizing controls were used. These controls optimized the development of the whole mesh on all the domains, thus allowing for the refinement of the mesh on curvatures and gap proximities. Moreover, the controls limited the maximum size of the elements up to the values showed in Table 2. The global sizing controlled the growth rate of the entire mesh with a ratio of 1.2 as well. This meant that the grid was gradually coarsened from the refined zones with a ratio of 1.2 up the maximum values fixed in the global settings. Due to the
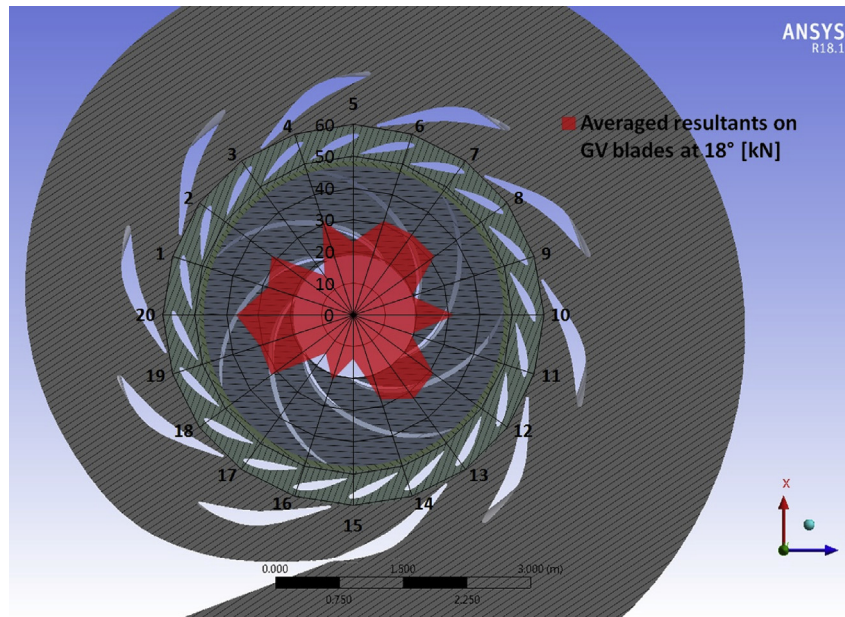
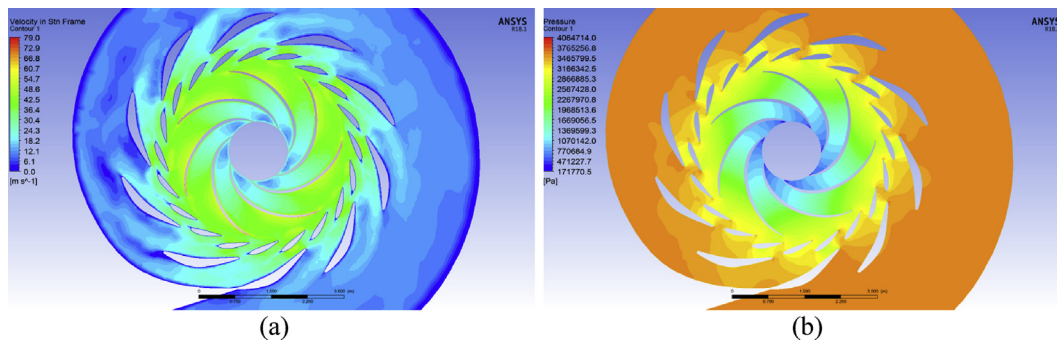**Fig. 6.** Magnitude of the time-averaged resultants on each GV blade for an opening angle of 18°.

Fig. 7. Contours of instantaneous velocity magnitude (a) and relative pressure (b) at a mid-span section for GV blade opening angle of 18°.

complexity of the geometries, tetrahedral elements were used for all the domains except for the draft tube, as mentioned. For the impeller a volume sizing control was superimposed to the global control in order to force the generation of a finer mesh according to the maximum values reported in Table 2. Furthermore, as the rotation was modeled by using an unsteady sliding mesh model, the mesh at the interfaces between rotor and stator vane was set in such a way to have identical element dimensions, therefore reducing the interpolation errors. As far as the GV domain was concerned, three specific refinement controls were applied. A volume sizing, a face sizing over the blade surfaces and an inflation which generated prismatic layers over the blades. The inflation layers improved the resolution of the boundary layer gradients. Finally, Grid 1 was the coarsest one without inflation layers. Grid 2 was the intermediate one, with five inflation layers. Grid 3 was the finest one with ten inflation layers.

In Fig. 3 details of the mesh for the condition with GV opening equal to 18° are presented. These details refers to Grid 2 which is the one used in the present work. Indeed, from the results presented in Table 2, this grid was the best compromise between accuracy and calculation time when used with a time step of 0.0004 s, corresponding to an angular step of approximately 1 deg.

2.2. CFD solver settings

The CFD model settings are reported in Table 3. As aforementioned, it

was an unsteady RANS model of the full reversible turbine under pumping operating conditions. The sub-iterations per time step were chosen in such a way to ensure that all the residuals were below 10^{-4}. A pressure based solver with SIMPLE algorithm for pressure-velocity coupling was used. The pressure based solver was the suitable one for incompressible flows, such that in the present work, while the SIMPLE scheme, which solved the pressure and velocity equations in a segregated way, was chosen for its robustness, numerical stability and low computation requirements [6, 7, 8, 9, 10, 11, 12, 13, 14, 17, 18, 19, 20, 21]. Second order schemes were used for the spatial and temporal discretization as they represented a good compromise between high numerical accuracy and calculation time. The relaxation factors were reduced as showed in Table 3 in order to improve the solver stability thanks to a more gradual iterative process. For the simulation of the impeller, an unsteady sliding mesh model was used in order to take into account for the stator-rotor interaction. As aforementioned in the reviewed literature [6, 7, 8, 9, 10, 11, 12, 13, 14], the unsteady RANS equations with k-ε turbulence closure represented a good compromise for the scope of the present work in terms of accuracy and computation times. Specifically, the RNG k-ε model, with standard wall function, demonstrated high reliability for the swirling dominated flows. Indeed, the RNG k-ε model had specific modifications for effective viscosity and swirling flows which appeared to be particularly suitable for Francis turbine simulations [17, 18, 19, 20, 21]. The solution initialization conditions were automatically established by the Fluent hybrid
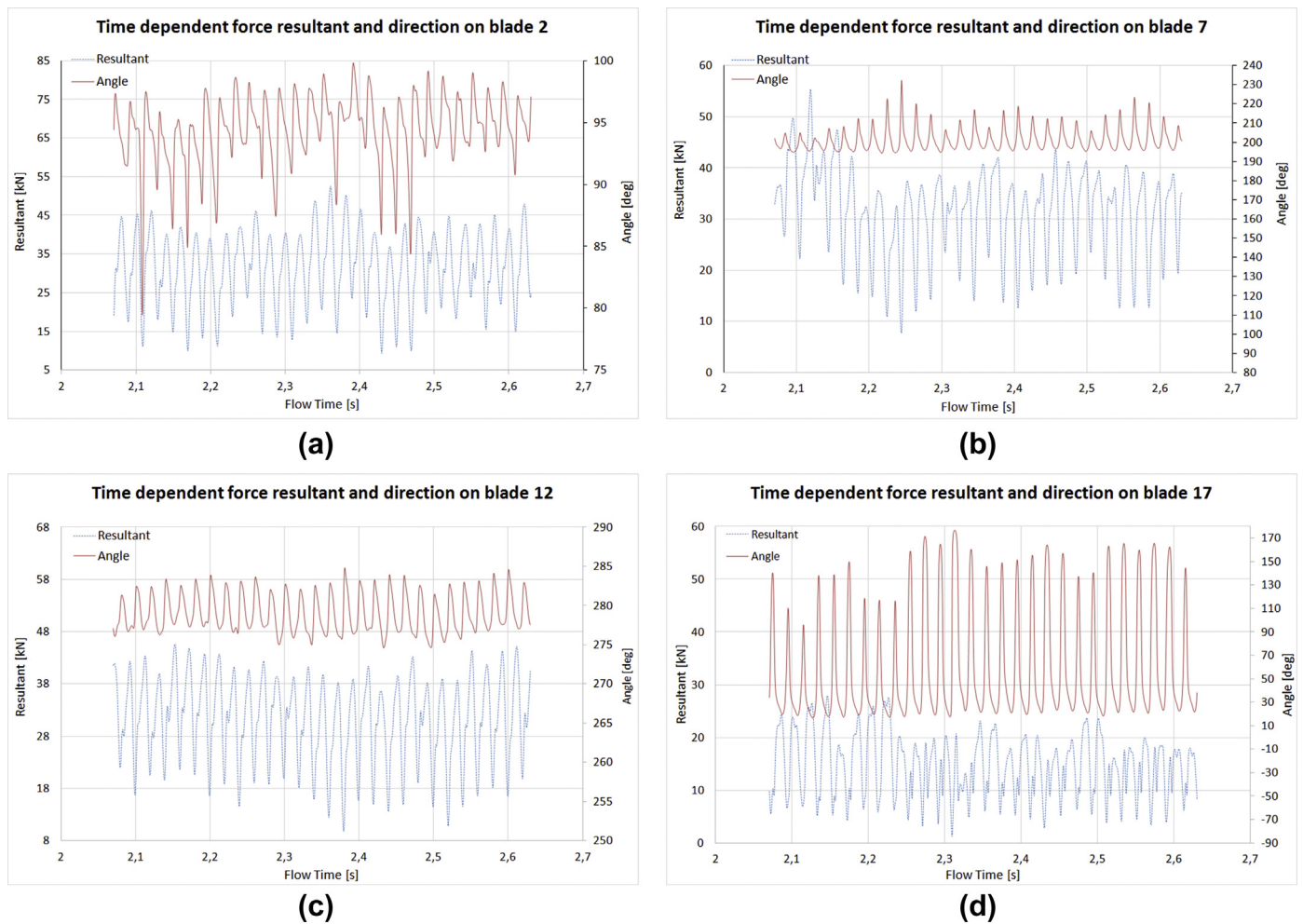
Fig. 8. Time dependent sampled trend of force resultant R and direction angle θ for blades 2 (a), 7 (b), 12 (c), 17 (d) for GV opening angle of 18°.

initialization method which performed ten pre-iterations basing on the boundary conditions provided in Table 3. In this way, a more accurate initial condition was provided therefore allowing for a faster convergence. In addition to what is shown in Table 3, the gravity in the z direction was activated. Further clarifications regarding the boundary conditions must be made. Indeed, since the experimental pressure measurements at sections S_1 and S_2, for the specific simulated operating conditions, were available, these values were used through the definition of a pressure inlet at section S_2 and a pressure outlet at section S_1. These measurements represented the real pressure head during the experimental operating condition, therefore they taken into account for the load losses and the real hydraulic circuit in which the Francis turbine operated. Compared to the use of a mass flow inlet boundary condition, these boundary condition definitions were certainly more appropriate and realistic, in consideration of the final goal of this work which was to evaluate the hydrodynamic instabilities due to the variable loads over the GV blades. In this way, the validation of the model was made by comparing the numerical and experimental fluid dynamic power and the mass flow rate, as showed hereinafter. For the turbulence boundary conditions, Fluent default values were used as they represented a fully developed turbulent condition very close to the real turbulent conditions within the ducts. In Fig. 4 the boundary condition type are specified on the CFD domain.

2.3. Experimental validation of the model

Regarding the validation of the model, ENEL provided a set of experimental data which are comapred to the numerical results in Table 4. Specifically, these are the aformentioned pressure head at sections S_1 and S_2, the measured mass flow rate and absorbed hydraulic power, obtained from the electrical absorbed power, knowing all the related efficiencies. All these data were measured in a real pumping operating condition with a GV opening angle of 18°, from the full closed position, at a constant rotational speed of 428.57 r/min. Furthermore, in Table 4, the calculated average velocities at inlet and outlet are reported and compared to the measured one.

As shown in Table 4, the comparison between the experimental and the simulated test case data demonstrates the excellent accuracy of the CFD model. The relative error between calculated and measured mass flow rate is less than 1% while the relative error on hydraulic power is less than 2%. Moreover, the simulated and the measured velocities at inlet and outlet are in very close proximity. Thus the CFD model can be considered accurate and reliable for the purposes of the present work. The final goal of this paper was first to identify the temporal trend and the intensity of the loads which act on the GV blades under the real test case condition. Subsequently, using exactly the same meshing strategy and model set up, the effects of the guide vane opening angle on loads and efficiency were evaluated in order to verify the possibility to have a reduction of the unsteady loads while keeping high hydraulic efficiency.

In order to check the convergence, some monitors were activated. A monitor for the residuals of the iterating process which ensure that the prescribed number of sub-iterations led to residuals below 10^{-4}; a monitor for the mass flow rate at outlet; a monitor for the torque, which allowed for the sampling of its oscillating temporal trend; fourty
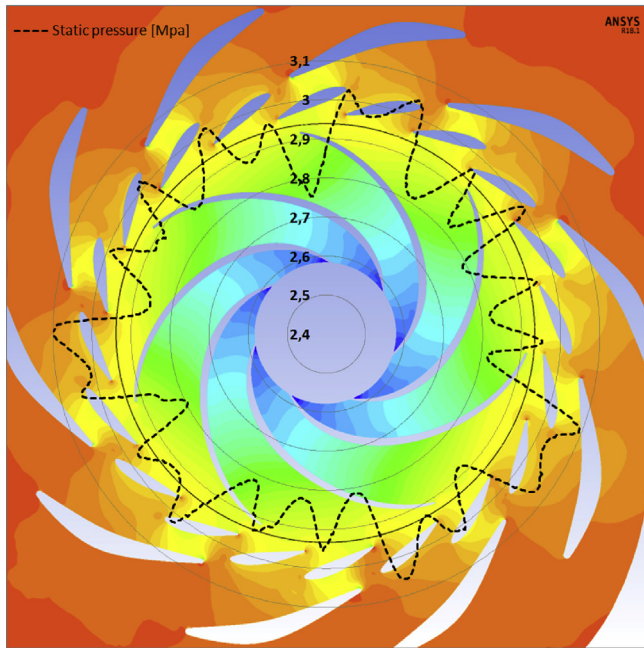
Fig. 9. Azimuthal static pressure distribution at a constant radius (black circle at a mid-span section) within the rotor-stator interface for GV opening angle 18° superimposed on instantaneous static pressure contours at the same mid-span section.

monitors, two for each guide vane blade, which allowed for the sampling of the oscillating time dependent forces in the 2D cartesian directions. The simulations converged when all the monitored quantities predented an approximately constant time dependent oscillating trend and, at the same time. This required form 3 to 5 complete rotor revolutions. Then the

quantities were sampled for four consecutive rotations for the following post-processing analysis. All the details about the results are reported in the next section.

All the simulations were carried out in ANSYS Fluent, within ANSYS Workbench 18.0, on a HP Z820 workstation with 128 Gb of RAM memory and two Intel Xeon E5-2695 processors with six cores for each and 24 available threads, taking advantage of the parallel computation.

3. Results and discussions

The first part of the post-processing analysis is dedicated to the evaluation of the experimental test case simulation. Then the parametric study on the GV blade opening angle is presented.

In order to extrapolate the forces which act on each guide vane blade, the frame of reference reported in Fig. 5 was used. In this way the time-averaged forces in x direction (F_x) and z direction (F_z) were sampled using the specific monitors generated in ANSYS Fluent. Thus the resultant of the hydrodynamic forces R and its direction θ were obtained. The frame of reference was obviously equal for all the blades and for all the other simulations as well.

3.1. Post-processing analysis for on-design condition (GV opening 18°)

The time-averaged resultants for each GV blade, obtained after four impeller revolutions, are shown in Fig. 6. Fig. 6 was obtained over-imposing a polar chart on a mid-span turbine section in order to specify the blade numbering which was the same for the following parametric study. The polar chart reports the numbering of the blades, from 1 to 20 and the magnitude of the time-averaged resultant forces in kN. In this way the behavior of the time-averaged loads, blade by blade, is immediately evident. The even GV blades are those closest to the SV blades and form a sort of duct with them. The odd GV blades are instead far from the SV blades, approximately within the SV ducts. This generates a different hydrodynamic behavior which has an impact on the loads distribution on each blade. In principle, in Fig. 6 the even blades present
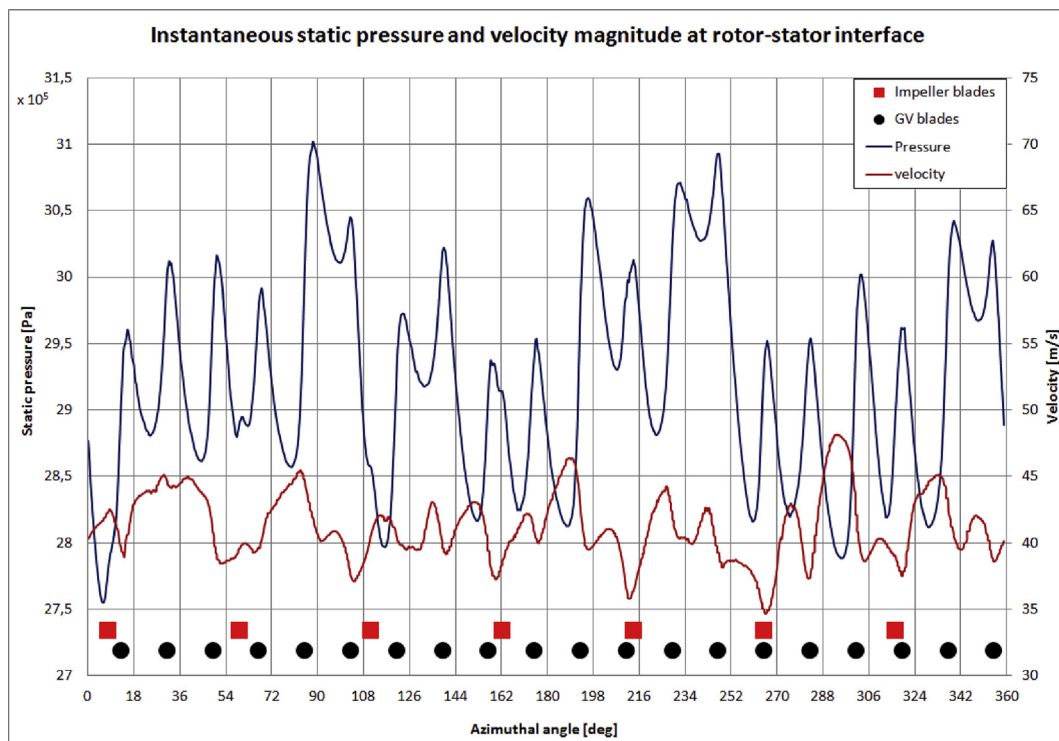

Fig. 10. Azimuthal static pressure and velocity magnitude distribution at a constant radius within the rotor-stator interface for GV opening angle 18°. Red squares are the trailing edge impeller blade positions. Black dots are the trailing edge GV blade positions. Radius and instant of time equal to Fig. 9.
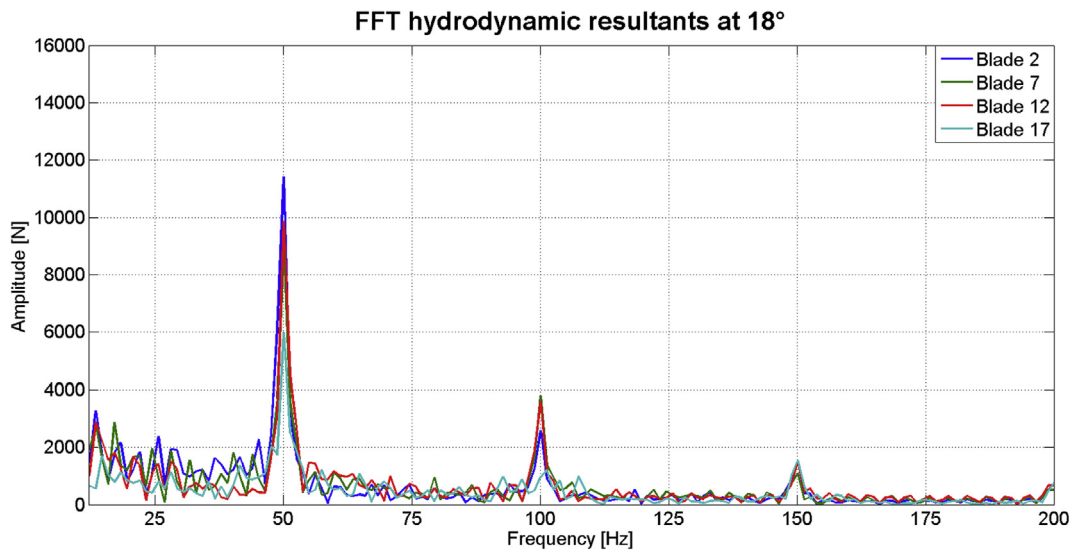
Fig. 11. Fast Fourier transform of the time-dependent hydrodynamic resultant magnitude for blades 2, 7, 12, 17 (see Fig. 6 for reference).
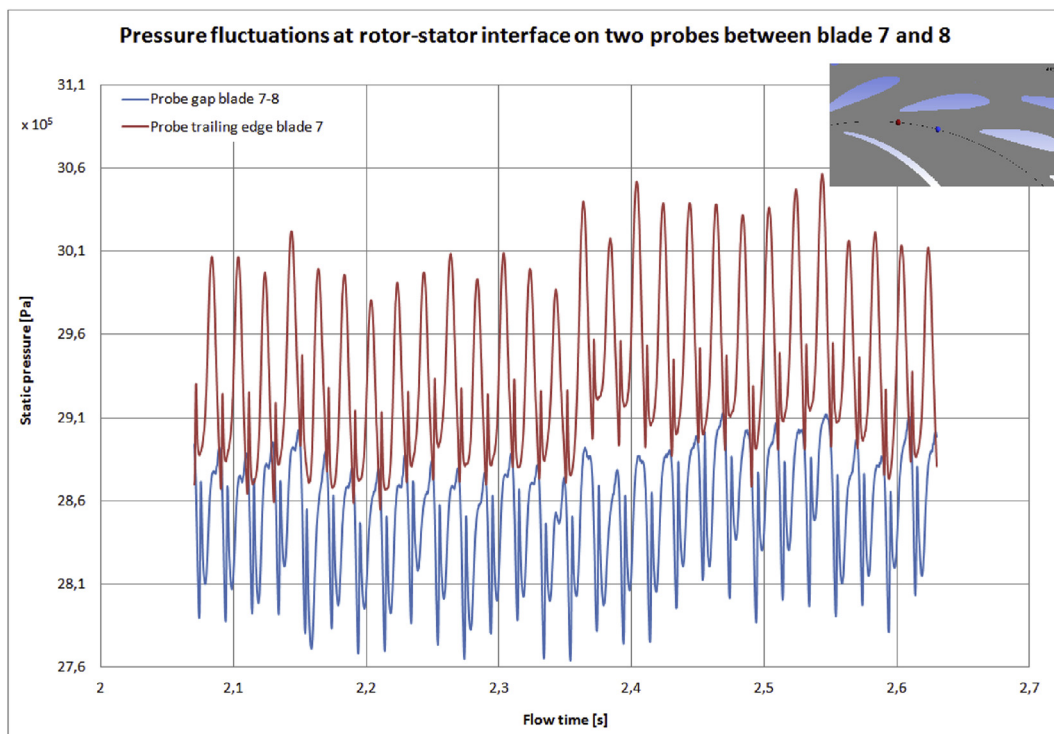

Fig. 12. Time-dependent pressure fluctuations sampled on two probes at a circumference within the rotor-stator interface at a mid-span for GV opening angle 18°, for two consecutive azimuthal positions. Red line refers to a probe near the trailing edge of blade 7. Blue line refers to a probe placed on the gap between blade 7 and 8.

higher average loads. For example, blade 2 shows an average load higher than 30 kN while blade 3 is below 20 kN. However, this phenomenon does not occur for all the blades.

In order to try to understand the causes of such a behavior, the instantaneous velocity magnitude and pressure contours are post-processed in Fig. 7. Here, due to the proximity to the SV blades, the even blades are subjected to local flow acceleration which implies a local different pressure distribution compared to the odd blades. On average, this means that the even blades are subjected to higher loads due to the overpressure generated by the flow interaction within the gap between GV blade and SV blade. However, although this provides a good explanation for the general differences between even blades and odd blades, it

does not allow for the comprehension of the behavior of the average loads on blades 7, 13 and 19 which show values comparable to the even blades. It can be supposed that there are specific fluid dynamic phenomena which have frequencies such that some blades are constantly overloaded compared to the others. For example mass oscillations, vortex shedding or similar. However, it is very arduous to understand and single out these phenomena in this simulation. What clearly appears in Fig. 6 and Fig. 7 is the fact that the proximity between SV blades and GV blades generates a local constant overload due to flow acceleration and different pressure distribution.

In order to analyze in more detail the instantaneous loads which acts on the GV blades, in Fig. 8 the temporal trends of the resultant force
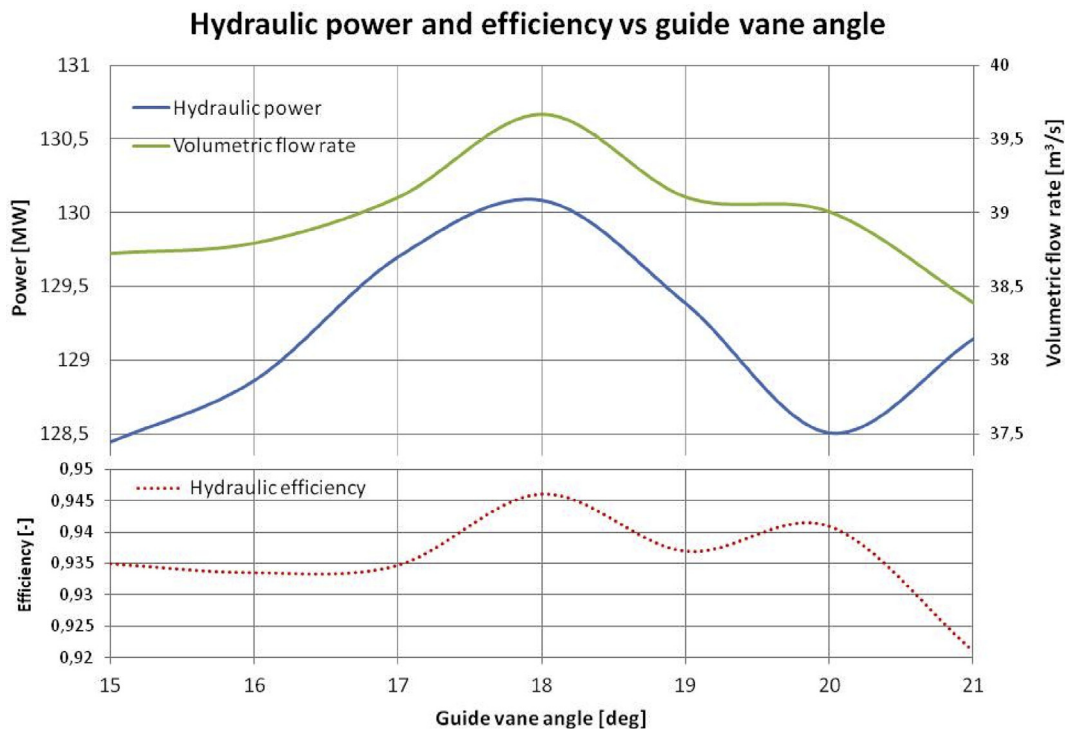
Fig. 13. Trend of hydraulic power, efficiency and volumetric flow rate as a function of the GV blade opening angle.

magnitude R and angle θ are presented. The data are sampled for four complete impeller revolutions for two odd blades and two even blades at different positions within the GV. These data are significant for all the other GV blades as well. Recalling the frame of reference in Fig. 5 and the blades numbering in Fig. 6 the following considerations can be deduced. The magnitude of the instantaneous hydrodynamic resultant shows a noticeable oscillating trend for all the blades analyzed, approximately between 5 and 45 kN. At the same time, an oscillation of the direction angle is evident, more or less for all the blades. Both these phenomena certainly represent a considerable source of fatigue for the mechanical resistance of the pins and the support bushings of the blades. Some blades, like blade 2 and 17, present higher oscillations of the direction angle, other blades, like blade 7 and 12, show lower oscillations of the direction angle. An explanation for this peculiarity is not easy to find. It could be local unsteady phenomena that are difficult to identify even with such advanced fluid dynamics simulation. In this regard, a more detailed CFD analysis of the blade cascades will be carried out in future works.

However, based on the study of Ubaldi et al. [22], further investigations on the flow structure within the rotor-stator interface were made. Specifically, in Fig. 9, a polar chart shows the instantaneous azimuthal static pressure distribution sampled in a circumference (black circle in Fig. 9) within the rotor-stator interface at a mid-span section. The polar chart was superimposed to the instantaneous pressure contours, at the same mid-span section, in order to evidence, in a clear way, the exact position of rotor and stator with respect to the polar trend of the static pressure. Furthermore, the contours allowed for meaningful contextualization of the pressure trend within the global pressure field.

Fig. 9 demonstrates that the gap between rotor and GV blades is affected by pressure fluctuations of some significance. These fluctuations are generated by the interaction between the flow from the impeller and the GV blades. Specifically, low pressure areas are located in proximity of the intrados of the GV blades. This occurs up to the area in proximity of the gap between two consecutive GV blades. In this area a pressure rise is evidenced and is probably due to the diffusion generated by the gaps between the GV blades. The pressure rise caused by the diffusion, is

evidently propagated within the impeller-GV blade gap. Furthermore, the rotor blade passage seems to emphasize the spatial pressure fluctuations.

The same instantaneous pressure trend is reported in the chart of Fig. 10 together with the velocity magnitude distribution obtained at the same circumference. The angular position of the trailing edges of rotor and stator blades is reported as well. The analysis shows a relation between pressure and velocity. Specifically, areas of low pressure correspond to areas of high velocity and vice versa. Furthermore, close to the impeller blades, areas of low velocity are evident and demonstrate the blade passing effect. This confirms that the rotor-stator interaction flow structure represents an important source of unsteadiness and instabilities due to a complex pressure and velocity spatial distribution which affect the GV blades unavoidably.

The above demonstrates the analytical potentialities of the proposed CFD model. Detailed fluid dynamic analyses, like those reported, are not possible through experimental investigations and they allow for a thorough investigation of the main sources of hydrodynamic instability which involves structural fatigue and mechanical wear of the materials. In this regard, a Fast Fourier Transform (FFT) analysis of the time dependent resultant magnitudes, for the blades of Fig. 8, was carried out using a default Matlab script. The results are reported in the chart of Fig. 11.

The FFT spectral analysis allows for the detection of the main frequencies of the hydrodynamic forcing signal on the blades and their relative amplitudes. Due to the limited sampling period (four revolutions or 0.56 s) the frequencies below 7 Hz (which correspond approximately to one revolution) are filtered in such a way to reduce the possible artificial detection of low frequencies which would require much longer sampling periods. The forcing evidenced at 50 Hz and multiples are interesting due to the fact that they are related to a specific phenomenon which might be the most important source of fatiguing of the GV blades. Being the rotational speed of the impeller $n = 428.57$ r/min, the frequency of rotation will be 7.1428 Hz. As the impeller has 7 blades, the frequency of the rotor-stator blade interaction, named as "blade passing frequency" will be exactly 50 Hz. The forcing detected at 50 Hz in Fig. 11
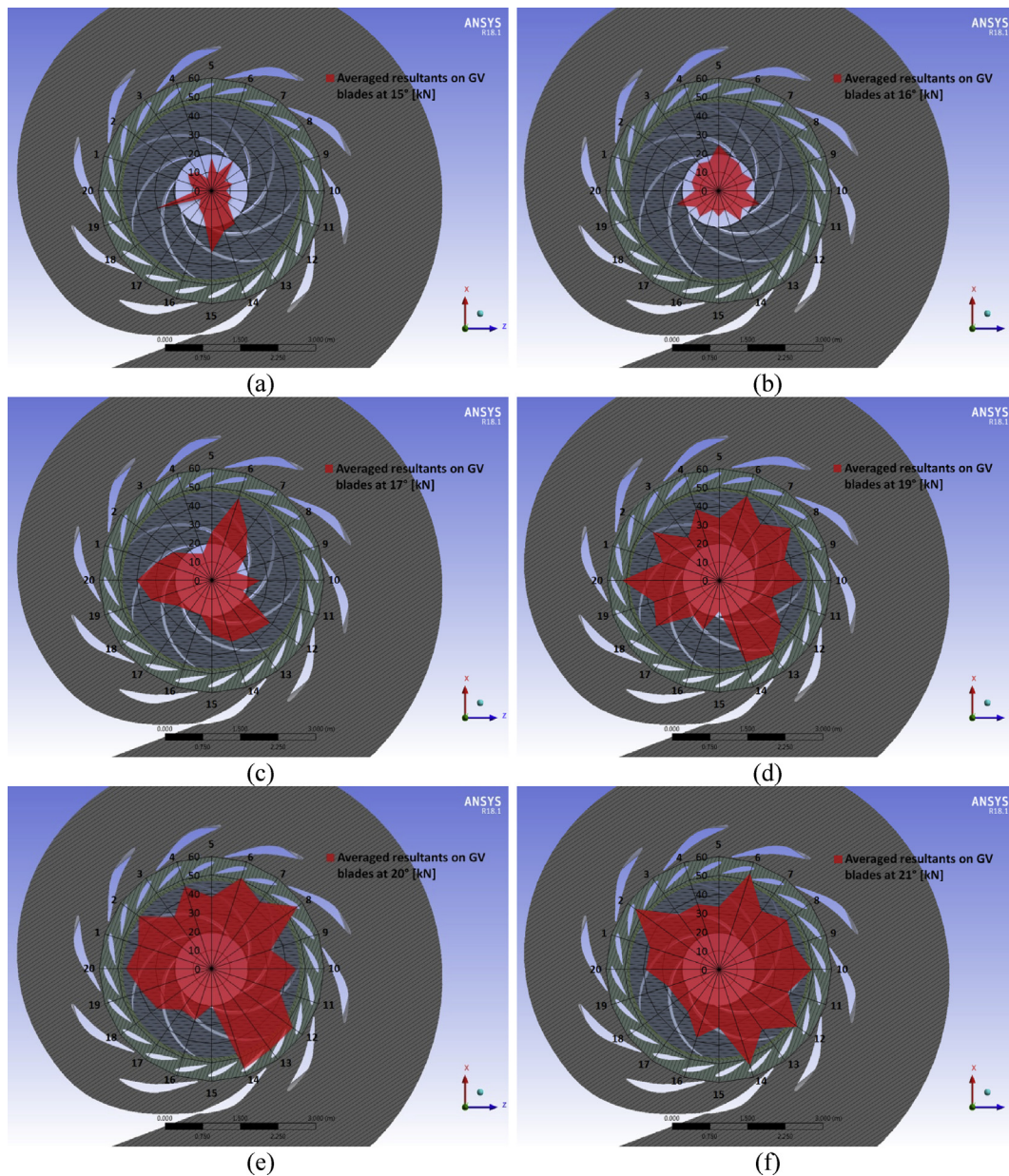
Fig. 14. Magnitude of the time-averaged resultants on each GV blade for opening angles of 15° (a), 16° (b), 17° (c), 19° (d), 20° (e) and 21° (f).

is therefore due to the pressure and velocity fluctuation caused by the impeller blade passing.

Finally, in Fig. 12 the time-dependent pressure fluctuations on two probes are shown. The probes were defined on the same circumference within the rotor-stator interface as that of Fig. 10. One probe was placed in proximity of the trailing edge of blade 7, the other probe was in the middle of the gap between blade 7 and blade 8 as evidenced in the box at the top right of Fig. 12. The static pressure data were sampled for four consecutive revolutions. The choice of the blades for the positioning of the probes was not relevant as the results were similar for all the blades in term of frequency of oscillations. Fig. 12 shows that, on average, the pressure at the GV blade trailing edge proximity is higher than that between two consecutive blades. This confirms, in the time domain, what is found in Fig. 9 for the instantaneous spatial distribution. The presence of the GV blades generates an irregular spatial pressure distribution within the rotor-stator interface which is constant in time. However, Fig. 12 shows time-dependent fluctuations as well. These fluctuations are due to the impeller blade passing. Indeed, very similar results of that in Fig. 11 were

found by carrying out a spectral analysis of the pressure signal in Fig. 12.

The above demonstrates that the presence of the GV blades causes an irregular pressure distribution in space while the rotor blade passing generates strong pressure fluctuations in time within the rotor-stator gap. Both these phenomena certainly represent a source of instability. Mostly, the blade passing frequencies at 50 Hz and multiples represent highly fatiguing conditions for the GV blade structure. ENEL monitored the vibrations on the GV blades by means of vibrations transducers and they found main forcing at exactly the same frequencies of the hydrodynamic analysis proposed here. Specifically, 50 Hz and multiples were found to be the most important frequencies. The vibration analysis cannot be reported due to proprietary reasons, however these results supported the validity of what was found in this work. Therefore, the frequencies of 50 Hz and multiples are intrinsic forcing of this machine which will never be completely eliminated. However, the intensities of all the frequencies in Fig. 11, including this fundamental 50 Hz, might be reduced by changing the GV opening angle. For this reason the aforementioned parametric analysis was made and is reported in the next sub-section.
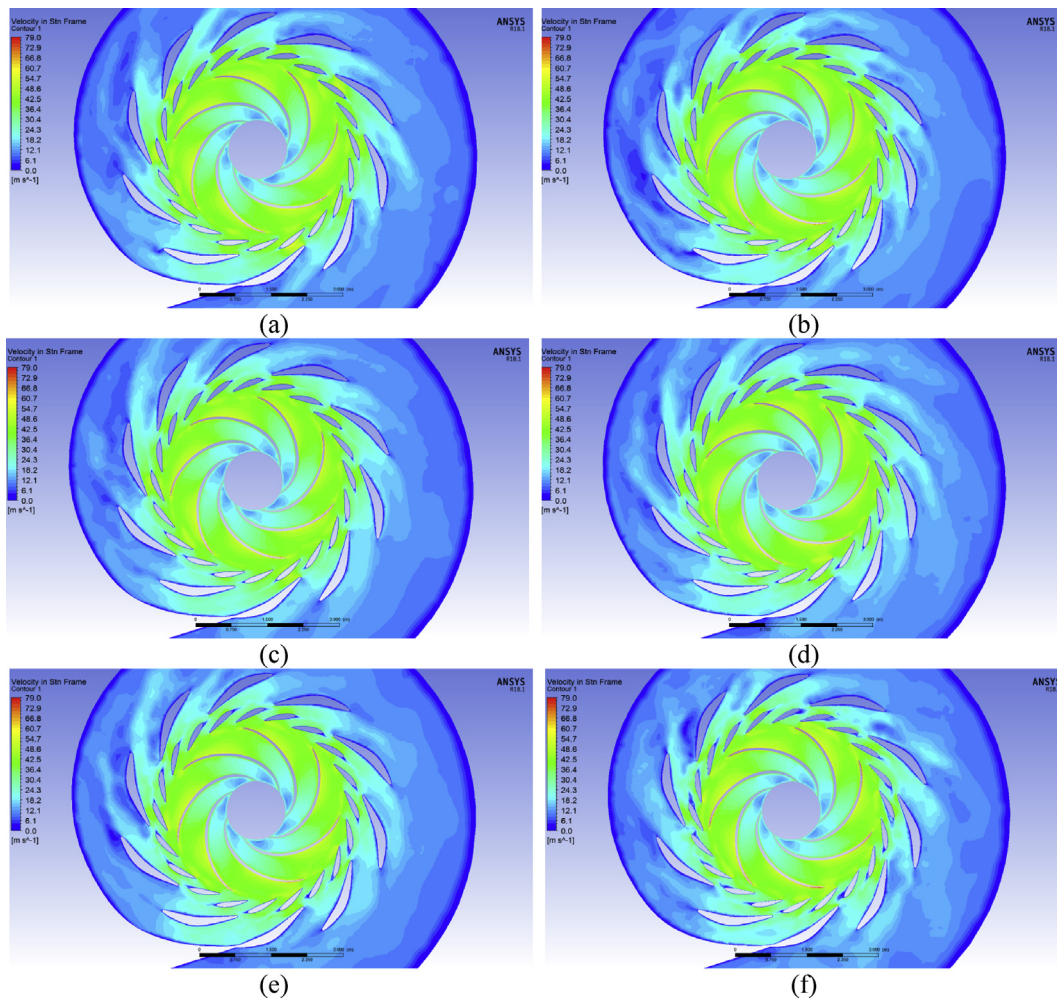
Fig. 15. Contours of the instantaneous velocity magnitude at a mid-span section for 15° (a), 16° (b), 17° (c), 19° (d), 20° (e), 21° (f) GV blade opening angles.

3.2. Post processing of the GV opening angle sensitivity study

As aforesaid, using exactly the same modeling strategy used for the test case simulation a parametric study was carried out. The boundary conditions were the same as well. The simulated range of GV blade opening angles was 15°, 16°, 17°, 19°, 20° and 21° with respect to the full closed position. Also in this case, after having reached the convergence, the data were sampled for four consecutive impeller revolutions and then time-averaged and post-processed.

In Fig. 13 the trend of the most important fluid dynamic parameters, at different GV opening angles, under pumping operating condition, are shown. These data are the time-averaged results of the CFD simulations. It is evident that the on-design condition, with an angle of 18°, is the one that maximizes absorbed power and efficiency. This means that the fluid dynamic design was very accurate and aimed at maximizing the efficiency. The volumetric flow rate trend is similar as expected, due to the fact that the GV in this machine is the device which regulates the flow rate. However, a part from the high opening at 21° in which the performance decrease, the other opening angles lead to acceptable efficiencies, between 0.93 and 0.94 against 0.946 in the best condition at 18°. This would allow for a margin of regulation that, at the expense of a slight performance reduction, might reduce the hydrodynamic stresses on the GV blades.

For this purpose, the magnitude of time-averaged resultant forces on GV blades at different opening angles are reported in the charts of Fig. 14. These charts were obtained through the methodology of Fig. 6, using the same blade numbering and scale in order to have a significant

comparison. Globally, the magnitude of the time-averaged resultants evidently increases as the opening angle increases. This is due to the fact that, as the opening angle increase, the angle of attack of the blade increases and, as a consequence, the hydrodynamic forces increase in magnitude. Therefore, higher opening angles lead to higher loads over the GV blades while lower angles lead to lower loads. However, analyzing the opening angles below 18°, which would lead to a desirable loads reduction, some peculiarities are evidenced in Fig. 14. At 15° the average resultant distribution over the blades appear irregular with some blades with very low loads and other blades, like 13, 14, 15 and 19 with high loads.

An explanation for this particular behavior is not easy to find. At 16° the resultant distribution appears to be more regular with values between 10 and 20 kN. At 17° the average loads increase up to over 40 kN and three areas of higher force are evident, approximately near blade 6, 13 and 20. Moreover, the aforementioned effect of the SV-GV interaction seems to be different at 15° and 16° while it begins to appear at 17° and it becomes increasingly evident at higher angles. This is due to the change in the shape of the gap generated by the different angular position of the GV blades with respect to the SV blades. This evidently changes the flow-field and the pressure distribution inside the GV-SV gap therefore causing a different distribution of the loads when the GV angle changes.

In order to analyze the fluid dynamic behavior when the GV opening angle changes, the contours of instantaneous velocity magnitude and relative static pressure are reported in Fig. 15 and Fig. 16. Fig. 15 shows the field of velocity at the different GV opening angles. It is evident that as the angle increases the flow impacts the GV blade profile in a different
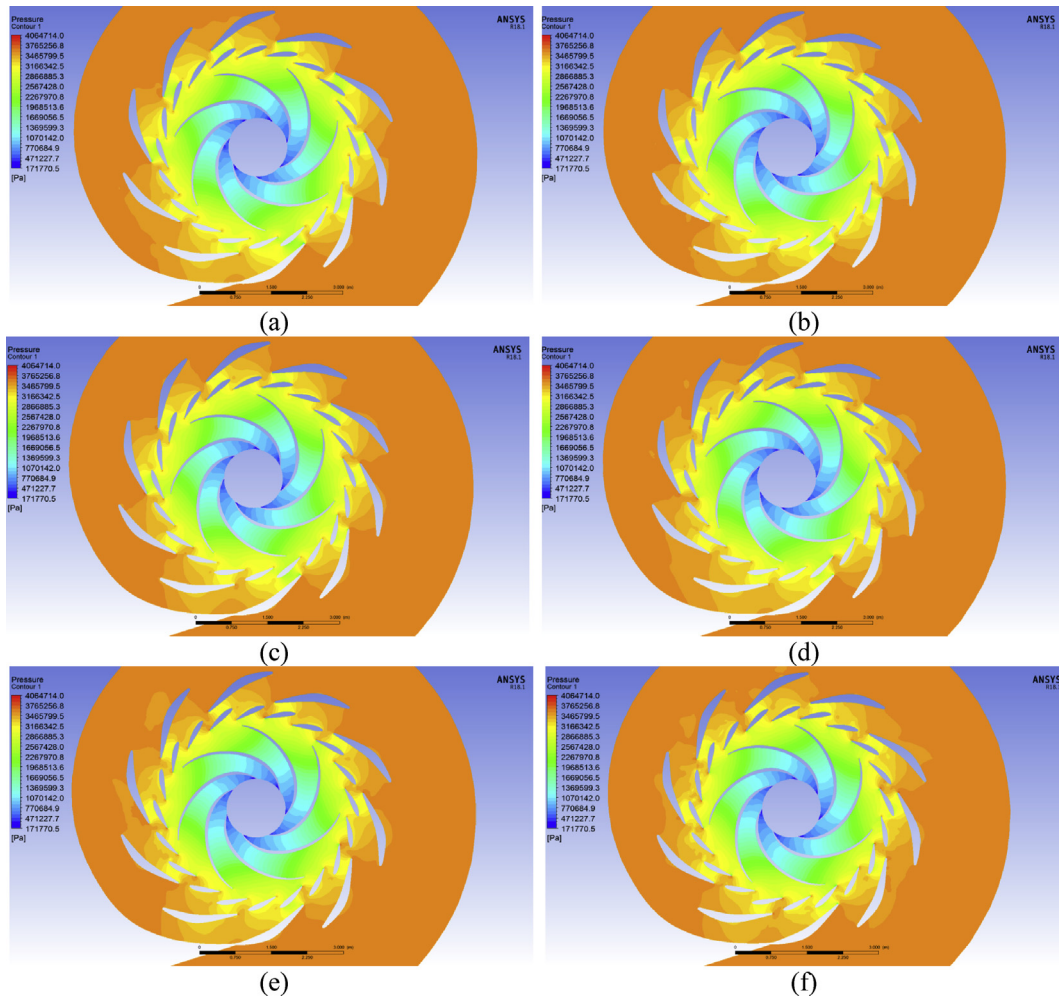
Fig. 16. Contours of the instantaneous relative pressure at a mid-span section for 15° (a), 16° (b), 17° (c), 19° (d), 20° (e), 21° (f) GV blade opening angles.
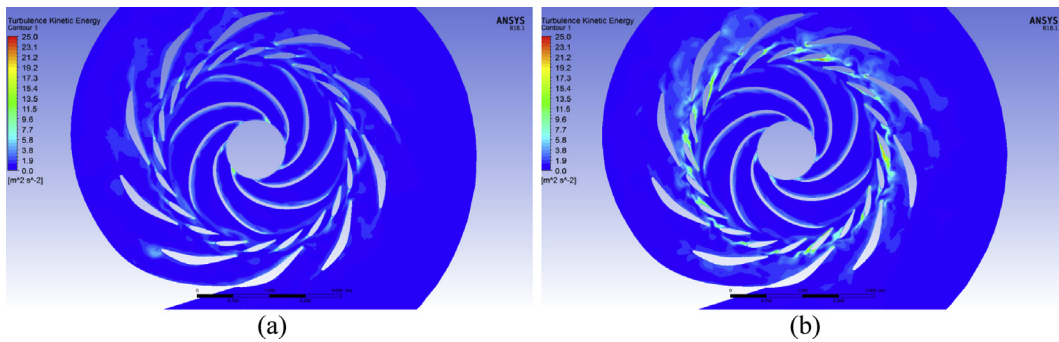

Fig. 17. Contours of instantaneous turbulent kinetic energy at a mid-span section for 15° (a) and 21° (b) GV blade opening angles.

way and the interaction between GV and SV blades and between GV blades themselves considerably changes. At 15° the flow seems to be quite aligned to the GV blade cord. As the GV angle increases the angle between flow and GV blade chord increases and the flow impact on the extrados of the GV blade profile.

At 21° this is quite evidenced by the small recirculation area near the leading edge of all the GV blades. Furthermore the velocity due to the SV-GV blade interaction seems to decrease at high angles. The fact that the flow impact with an increasing angle the extrados of the GV blade profile provide an explanation for the force increment evidenced in Fig. 14.

Indeed this causes an increasing dynamic pressure over the GV blades which further pushes inwards, in the direction of the impeller. This dynamic pressure is added to the strong pressure generated by the spiral diffuser. At low angles the dynamic pressure is noticeably reduced and the higher flow acceleration within the SV-GV blade gap rather causes a pressure drop which locally reduces the loads over the even blades. This would explain the reason why a different behavior of the SV-GV blade interaction is evidenced in Fig. 14. Moreover as the GV blade angle increases, the gap between the GV blades themselves increases and generates higher local fluid diffusion and thus higher local pressure. The

above is confirmed by the instantaneous relative pressure contours in Fig. 16.

In Fig. 17 the contours of instantaneous turbulent kinetic energy show the noticeable differences between 15° and 21°, which represent the minimum and the maximum simulated opening angles. The turbulent kinetic energy production represents a source of losses and causes high chaotic unsteady loads over the blades. In Fig. 17 very high turbulent kinetic energy production is evident at 21°, compared to 15°. This confirms the fact that the flow at 21° is not correctly aligned to the blade cord therefore generating an incipient flow separation that should be avoided.

The spectral analysis of the time-dependent hydrodynamic resultant magnitude, at the different simulated GV opening angles, is presented in Fig. 18. The data sampled and analyzed refer to blades 2, 7, 12 and 17 as in Fig. 9. In this way a significant comparison is possible. The FFT analysis in Fig. 18 confirms what is found in Fig. 11. The main forcing frequencies are approximately the same, with that due to the impeller blade passing evidenced at 50 Hz and multiples. As expected, instead, the amplitude increases as the angle increases. This further supports the hypothesis that high GV opening angles are much heavier for the

mechanical resistance of the guide vane.

Finally, Fig. 19 shows a plot of the 3D streamlines of velocity magnitude for the on-design condition, with GV opening angle of 18°. The streamlines allow for the visualization of the 3D flow between the inlet and the outlet of the domain that is the draft tube inlet and the spiral case outlet under pumping operating condition. A strong swirling flow due to the rotation within the impeller is evident. A complex 3D swirling flow seems to affect the spiral case as well.

The results presented above demonstrate the importance of the use of accurate CFD models for a thorough analysis of the complex fluid dynamic behavior of turbomachineries like Francis turbines. The large number of details, provided by the CFD model, allows for the detection of the possible sources of hydrodynamic instability which are probably the most responsible factors for the fatiguing problems experienced on the GV blade structure. Mainly the unsteady flow structure within the rotorstator interface seems to be the most important source of fatigue for the GV blades. Furthermore, an optimization strategy which would allow for the reduction of the fatiguing loads is obtained thanks the CFD model proposed in this work. Moreover, the CFD results can be used as the basis
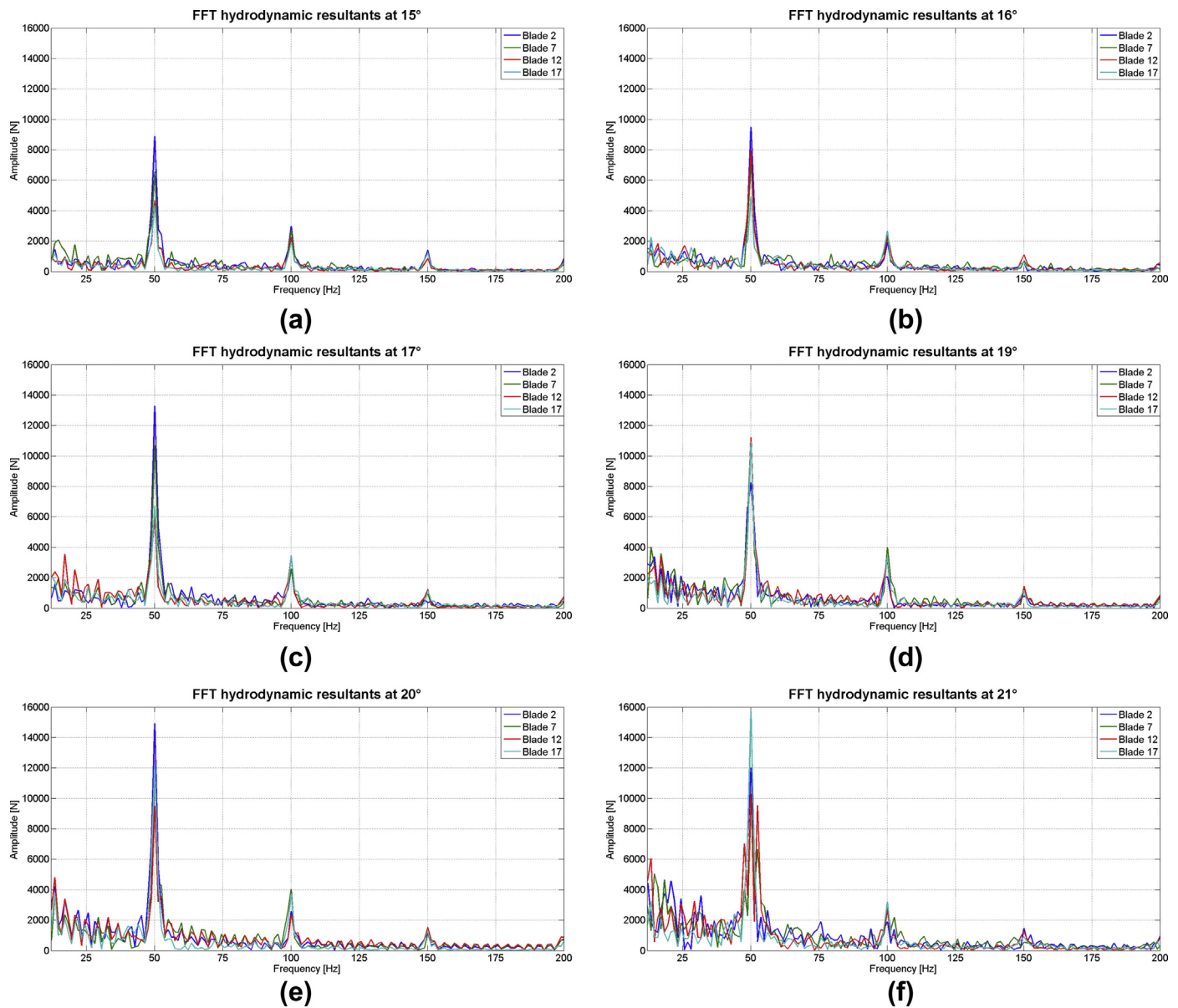

Fig. 18. Fast Fourier transform of the time-dependent hydrodynamic resultant magnitude for GV blade opening angles 15° (a), 16° (b), 17° (c), 19° (d), 20° (e), 21° (f) for blades 2, 7, 12 and 17 (see Fig. 11 for reference).
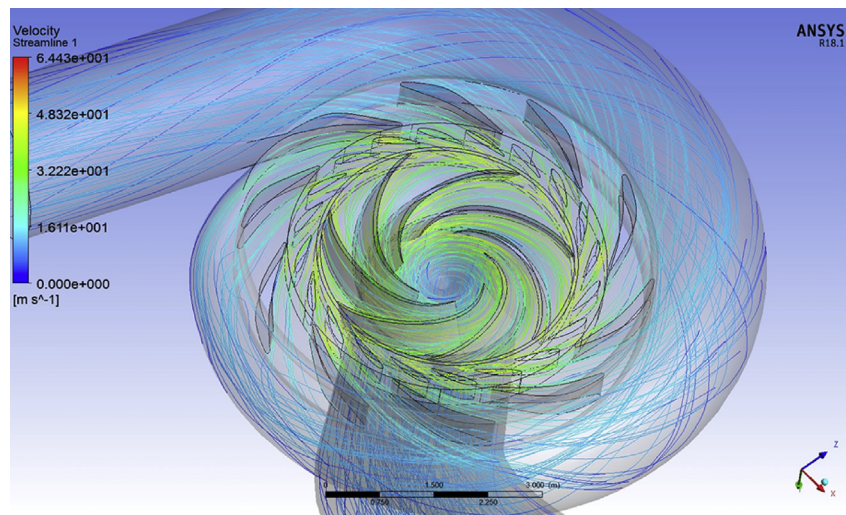
Fig. 19. 3D streamlines of instantaneous velocity magnitude for the on-design operating condition with GV opening angle 18°.

for the implementation of a fluid-structure interaction (FSI) model. The FSI model will use the temporal pressure field, provided by the CFD, for an accurate Finite Element Method analysis of the GV structure in order to find the most subjected areas to fatigue and the natural frequencies of the structure as well. Further CFD analyses about the vortex shedding influence will be made in future work [23, 24].

4. Conclusions

The work presented in this paper demonstrates the noticeable potentialities offered by the modern CFD for thorough analyses of specific fluid dynamic problems which otherwise would be very arduous to investigate. Specifically, starting from a real issue of the ENEL "Anapo" storage hydro plant, this paper shows how to develop and validate an advanced unsteady CFD model for the detection of the sources of the hydrodynamic instabilities in a Francis reversible turbine, under pumping operating conditions.

The specific boundary conditions of the proposed CFD model allowed for the precise simulation of a real pumping operating condition of the entire hydraulic system. This was of utmost importance in order to determine a realistic temporal trend of the hydrodynamic loads, which acted on the guide vane blades, as this area was subjected to the most important structural problems.

Through the use of an accurate post-processing analysis of the test case condition, performed at the on-design guide vane opening angle, the temporal trend of the hydrodynamic force intensities and their directions was obtained. This was one of the most important results that only a CFD model was able to provide as there were no experimental ways capable of easily providing such data. The results demonstrated that the guide vane blades were subjected to strong and highly oscillating forces which certainly represented an important source of mechanical stress for the guide vane structure. The use of Fast Fourier Transform for a spectral analysis showed that the guide vane blades were stressed by forces with various frequencies. The frequencies of 50 Hz and multiples were found to be characteristic frequencies of this machine. The thorough analysis of the flow structure within the rotor-stator interface showed that these specific frequency, usually known as "blade passing frequency", was due to the rotor-stator interaction. Furthermore, a strong flow interaction between stay vane and guide vane blades was detected. This interaction caused a further irregular pressure distribution over the guide vane blades which influenced the loads as well. The guide vane blades in proximity of the stay vane, in this operating condition, were subjected to higher loads.

In order to evaluate the effects of the angular opening of the guide vane blades, both on the performance of the machine and on the hydrodynamic loads, a parametric study was carried out. In this study the guide vane opening angle was varied while the CFD set-up and boundary conditions were exactly the same. The thorough post-processing analysis, showed that both the performance and the loads were quite sensitive to the guide vane opening. Angles higher than the on-design value led to high loads while lower angles led to lower loads due to a better flow alignment to the guide vane blades and a reduction of the pressure fluctuations. The FFT analysis confirmed the main forcing frequencies and the fact that lower angles reduced the blade loads. The stay vane - guide vane flow interaction was found for all the angles but with strong differences due to the change of the shape of the gap.

Finally, the results of the present study suggest that a slight reduction of the guide vane opening angle would be desirable to obtain a noticeable reduction of the fatiguing loads at the expense of a slight reduction of the hydraulic efficiency of system. A reduction from 18° to 16° would seem to be the best compromise.

The importance of this study is not only to contribute to the understanding of the internal fluid dynamics of the machine and the sources of instabilities. It represents the basis for a more detailed fluid-structure interaction analysis as well.

concerning the "Anapo" storage plant and the HydroArt/Riva Francis Turbine are exclusive industrial property of ENEL Green Power. Thanks to ENEL Green Power for providing the data, allowing access to the storage plant and proposing the study.

Additional information

No additional information is available for this paper.

References

[1] Ackermann, T. Impact of high wind penetration on balancing and frequency control in Europe IEEE Power Energy Mag. Volume 5, Issue 6, Pages 91-103 doi:.

[2] A. Dukpa, I. Duggal, B. Venkatesh, L. Chang, Optimal participation and risk mitigation of wind generators in an electricity market, IET Renew. Power Gener. 4 (issue 2) (2010) 165–175.

[3] L. Bayón, J.M. Grau, M.M. Ruiz, P.M. Suárez, Mathematical modelling of the combined optimization of a pumped-storage hydro-plant and a wind park, Math. Comput. Model. 57 (2013) 2024–2028.

[4] Á.J. Duquea, E.D. Castronuovo, I. Sánchez, J. Usaola, Optimal operation of a pumped-storage hydro plant that compensates the imbalances of a wind power producer Electric, Power Syst. Res. 81 (2011) 1767–1777.

[5] M. Parastegari, R.A. Hooshmand, A. Khodabakhshian, A.H. Zare, Joint operation of wind farm, photovoltaic, pump-storage and energy storage devices in energy and reserve markets, Electr. Power Energy Syst. 64 (2015) 275–284.

[6] L.A. Teran, F.J. Larrahondo, S.A. Rodrìguez, Performance improvement of a 500-kW Francis turbine based on CFD, Renew. Energy 96 (2016) 977–992.

[7] J. Nicolle, J.F. Morissette, A.M. Giroux, Transient CFD simulation of a Francis turbine startup, in: IOP Conf. Series: Earth and Environmental Science vol.15, 2012, 062014, 26th IAHR Symposium on Hydraulic Machinery and Systems.

[8] M.K. Shukla, V. Prasad, R. Jain, S.N. Shukla, CFD analysis of 3-D flow for Francis turbine MIT, Int. J. Mech. Eng. 1 (2 Aug 2011) 93–100. ISSN 2230-7699 MIT publications.

[9] R. Khare, V. Prasad, S. Kumar, CFD approach for flow characteristics of hydraulic Francis turbine, Int. J. Eng. Sci. Technol. 2 (8) (2010) 3824–3831. ISSN: 0975-5462.

[10] C. Trivedi, M.J. Cervantes, B.K. Gandhi, O.G. Dahlhaug, Experimental and numerical studies for a high head Francis turbine at several operating points, J. fluids Eng. ASME 135 (November 2013), 111102-1.

[11] J. Wu, K. Shimmei, K. Tani, K. Niikura, J. Sato, CFD-based design optimization for hydro turbines, J. Fluids Eng. ASME 129/159 (February 2007).

[12] H.J. Choi, M.A. Zullah, H.W. Roh, P.S. Ha, S.Y. Oh, Y.H. Lee, CFD validation of performance improvement of a 500 kW Francis turbine, Renew. Energy 54 (2013) 111–123.

[13] C. Trivedi, M.J. Cervantes, State of the art in numerical simulation of high head Francis turbines, Renew. Energy Environ. Sustain. 1 (20) (2016). EDP Sciences.

[14] S.R. Shah, S.V. Jain, R.N. Patel, V.J. Lkhera, CFD for centrifugal pumps: a review of the state-of-the-art, Procedia Eng. 51 (2013) 715–720.

[15] R. Lanzafame, S. Mauro, M. Messina, Numerical and experimental analysis of micro HAWTs designed for wind tunnel applications, Int. J. Energy Environ. Eng. 7 (2) (June 2016) 199–210.

[16] R. Lanzafame, S. Mauro, M. Messina, HAWT design and performance evaluation: improving the BEM theory mathematical models, Energy Procedia 82 (December 2015) 172–179.

[17] K.C. Anup, Bhola Thapa, Young-Ho Lee, Transient numerical analysis of rotor-stator interaction in a Francis turbine, Renew. Energy 65 (2014) 227–235.

[18] Lucien Stoessel, Hakan Nilsson Steady and unsteady numerical simulations of the flow in the Tokke Francis turbine model, at three operating conditions, J. Phys. Conf. Ser. 579 (2015), 012011.

[19] J. Li, J. Yu, Y. Wu, 3D unsteady turbulent simulations of transients of the Francis turbine, IOP Conf. Ser. Earth Environ. Sci. 12 (2010), 012001.

[20] Ying Hu, Heming Cheng, Ji Hu, Xirong Li, Numerical simulation of unsteady turbulent flow through a Francis turbine, Wuhan Univ. J. Nat. Sci. 16 (2) (2011).

[21] Shuhong Liu, Liang Zhang, Michihiro Nishi, Yulin Wu, Cavitating turbulent flow simulation in a Francis turbine based on mixture model, J. Fluids Eng. 131 (5) (May 2009).

[22] M. Ubaldi, P. Zunino, G. Barigozzi, A. Cattanei, An Experimental investigation of stator induced unsteadiness on centrifugal impeller outflow, J. Turbomach. 118 (1) (Jan 01, 1996) 41–51, 11.

[23] A. Ruprecht, O. Kirschner, F. Lippold, I. Buntic, Noise reduction in a small Francis turbine caused by vortex shedding at the trailing edge, numerical analysis and field test IAHR, in: 11th International Meeting of the Work Group on the Behaviour of Hydraulic Machinery under Steady Oscillatory Conditions, 2003. Stuttgart, Germany.

[24] T. Vu, B. Nennemann, P. Ausoni, M. Farhat, F. Avellan, Unsteady CFD Prediction of von Kármán Vortex Shedding in Hydraulic Turbine Stay Vanes Proceedings of Hydro 2007, Granada, Spain, October 2007, pp. 15–17.